The TES-based Cryogenic Anticoincidence detector for IXO: First results from large area prototypes

Claudio Macculi *[a], Luca Colasanti[a], Simone Lotti[a], Lorenzo Natalucci[a], Luigi Piro[a], Daniela Bagliani[b], Francesco Brunetto[b], Lorenza Ferrari[b], Flavio Gatti[b], Guido Torrioli[c], Paolo Bastia[d], Arnaldo Bonati[d], Marco Barbera[e], Giovanni La Rosa[f], Teresa Mineo[f], Emanuele Perinati[f]

[a]INAF/IASF Roma, Via del Fosso del Cavaliere 100, 00133 Roma, (Italy);
[b]Physics Department of Genova University, Via Dodecaneso 33, 16146 Genova, (Italy);
[c]Istituto di Fotonica e Nanotecnologie del CNR, Via Cineto Romano, 42 00156 Roma (Italy);
[d]Thales Alenia Space Italia S.p.A., s.s. Padana Superiore 290, 20090 Vimodrone, Milano, (Italy);
[e]Physics Department of Palermo University, Via Archirafi 36 I, 90123 Palermo, (Italy)
[f]INAF-IASF Palermo, Via Ugo La Malfa 153, 90146 Palermo, (Italy)

ABSTRACT

The technique which combines high resolution spectroscopy with imaging capability is a powerful tool to extract fundamental information in X-ray Astrophysics and Cosmology. TES (Transition Edge Sensors)-based microcalorimeters match at best the requirements for doing fine spectroscopy and imaging of both bright (high count rate) and faint (poor signal-to-noise ratio) sources. For this reason they are considered among the most promising detectors for the next high energy space missions and are being developed for use on the focal plane of the IXO (International X-ray Observatory) mission. In order to achieve the required signal-to-noise ratio for faint or diffuse sources it is necessary to reduce the particle-induced background by almost two orders of magnitude. This reduction can only be achieved by adopting an active anticoincidence technique. In this paper, we will present a novel anticoincidence detector based on a TES sensor developed for the IXO mission. The pulse duration and the large area of the IXO TES-array (XMS X-ray Microcalorimeter Spectrometer) require a proper design of the anticoincidence detector. It has to cover the full XMS area, yet delivering a fast response. We have therefore chosen to develop it in a four-pixel design. Experimental results from the large-area pixel prototypes will be discussed, also including design considerations.

Keywords: TES, Cryogenic Detectors, X-ray, SQUID, IXO.

1. INTRODUCTION

The IXO (International X-ray Observatory) [1, 2] is a joined (ESA/NASA/JAXA) mission aimed at studying some of the most fundamental topics in contemporary astrophysics and cosmology. One of the instrument on-board IXO is the XMS (X-ray Microcalorimeter Spectrometer). It is a Kilo-pixel imaging-array based on TES (Transition Edge Sensor; for a complete review see [3] and Ref. therein) microcalorimeter technology. It will provide high spectral resolution images in the 0.3-10 keV range with ~ 2.5 eV FWHM resolution in the center of the field. In order to meet the scientific requirements, in particular for faint point or diffuse sources such as clusters of galaxies, it is necessary to reduce the background in the detector by almost two orders of magnitude below the value expected in the IXO orbit. This will require a high efficiency and fast anticoincidence detector that will be discussed here. Such a detector is called "CryoAC": Cryogenic AntiCoincidence detector. For a very brief review about both XMS and CryoAC aspects see Ref. [4, 5]. The CryoAC baseline design is based on a thin layer (0.3-0.5mm) Si absorber where the energy deposited by particles is sensed by TES. The detector is located below XMS, at a distance < 3 mm, and covers an area of 36x36 mm^2, larger than the array.

*claudio.macculi@iasf-roma.inaf.it; phone 0039 06 49934658; www.iasf-roma.inaf.it

The detector is divided in 4 independent sub-detectors, each one with an area of 18x18 mm^2. This approach offers important advantages in two areas. By using the same TES-based sensor technology of the TES array reduces substantially interface problem (thermal, mechanical, electrical), in particular allowing the use of the same SQUID read-out. In addition, it offers the prospects of using the CryoAC as a hard X-ray detector at E>20 keV allowing, in combination with the top-layer microcalorimeter array, the simultaneous measurement of X-ray spectral features over a broad energy range.

We have now developed a series of prototypes [6], of increasingly larger area, and with different TES configurations and area, to acquire high confidence in the scalability of performances. Three kind of detectors have been tested, constituted by a Silicon absorber of different area and volume, but also with different number of TESes so covering a different area of the absorber. The absorber area of different batches of detectors are: 15mm^2, and 1cm^2, i.e. the second batch is 6 times larger than the first one (that, in turn, is 300x larger than a typical pixel). The performances of the detectors are consistent with the requirements, in particular the time constants and the energy bandpass. Though not critical for the purpose of the anticoincidence, we plan to achieve in the near future further improvements in performances, with particular regard to the energy resolution. Considering the consistency and predictability of the performances over such a large variation in area, we do not foresee any significant problem to achieve the area of the baseline design (3.2 cm^2).

2. REQUIREMENTS AND OPERATION REGIME

The high level requirement that the implementation of the CryoAC has ultimately to fulfill is that the residual (i.e. un-discriminated) particle background has to be lower than the requirement of $2 \cdot 10^{-1}$ cts cm^{-2} s^{-1} in the TES-array energy range (0.3-10 keV). By means of Background estimation and making use of GEANT4 simulations [7], this translates in the following Table 1 about the instrument requirements:

Table 1. Main CryoAC Requirements

Size:	36x36 mm^2 (segmented in 4 pixel, each 18x18 mm^2)
Thickness:	300-500 μm
Distance from XMS:	< 3 mm
Rejection efficiency for particles: **CryoAC veto + discrimination by XMS threshold**	> 99% (Combined with TES array E>10keV)
Rise Time constant:	< 30 μs
Time constant Decay:	< 300 μs (Goal)
Bandpass:	20 keV – 0.5 MeV
Electronics:	Standard FLL SQUID
Moderate Energy Resolution:	(Goal)
High Energy Response:	(goal)

To satisfy the requirements we have explored solutions to operate the detector mainly in the so called "A-thermal" regime [8, 9]. The main reason is that the duration of the a-thermal pulse is quite short (rise time constant lower than 1 μs, pulse duration of ~ few tens of μs) with respect to the thermal signal (time duration of several hundreds of μs), so enabling the detector as an extremely fast anticoincidence flag for XMS. This regime assures less constraints on design parameters. On the other hand, it is quite important to cover as much as possible and uniformly the absorber by TESes (i.e. increase the collecting area–over–absorber area ratio) to collect a large fraction of the a-thermal phonons since they propagate not diffusively (as the thermal component), but along privileged direction (crystal-axis) reflecting on the interfaces.

We have developed detectors operated in three regimes: mixed mode (AC-s1: high $G_{Si-bath}$ to decrease thermal time constant; single TES); pure a-thermal (AC-s2: area up-scaled from AC-s1; 4 TESes; wide area Al pads); pure thermal (AC-s3: very low R_N; wide area Al pads; fast component electronically dumped), so demonstrating also the control on the main design parameters, fundamental for scaling to the final breadboard of 18x18 mm^2.

Next sections show a review of the main results, then the conclusion.

3. DETECTOR DEVELOPMENT AND TEST RESULTS

The main geometrical and thermal properties of the developed detectors are shown in the next Table 2.

Table2. Physical parameters of the detectors. Notes: (1) at 100 mK. For Ir we take the value of C in the normal phase. (2) includes the collecting area of the Al pads, the total TES area is 6 mm^2.

Sample	Area Si (mm^2)	Thickness Si (μm)	Area TES (mm^2)	Thickness TES (nm)
AC-s1	16.5	300	3.7	90 Ir
AC-s2	100	380	18[2]	50 Ir
AC-s3	100	380	33[2]	250 Ir 30 Au

Sample	C_{Si} (pJ/K)	C_{TES} (pJ/K)	G (W/K)	T_C (mK)	ΔT_C (mK)	R_N (Ω)	α
AC-s1	2.5[1]	14[1]	2 10^{-8}	95	5	0.6	55
AC-s2	134	29	6·10^{-10}	180	8	13.5	100
AC-s3	50	99 (Ir + Au)	2.6·10^{-8}	132	2	0.05	245

3.1 Prototype Detector AC-s1

The picture of AC-s1 is shown in Fig. 1. Some physical and geometrical parameters are shown in Table 2.
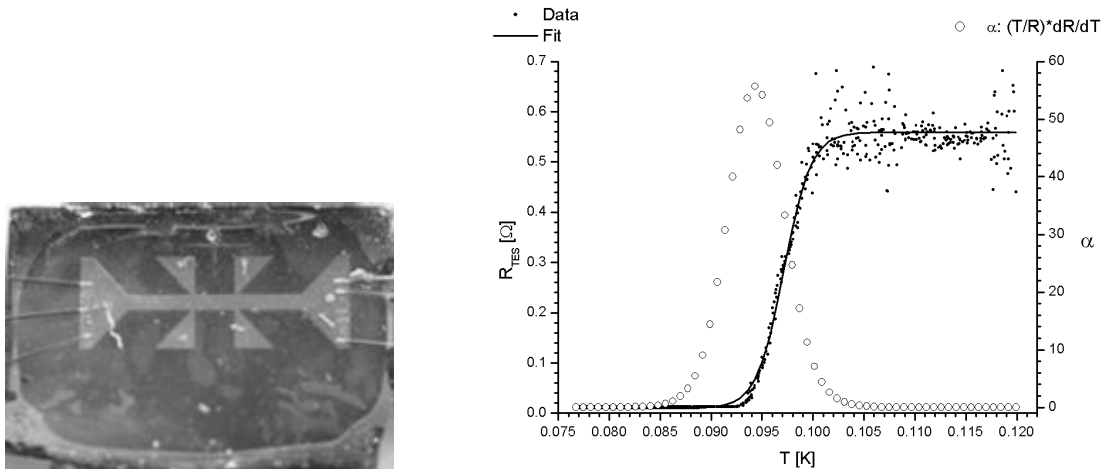

Figure 1. (Left) Photo of AC-s1. (Right) R-T transition. The line along the transition is a fit to evaluate alfa (open points).

The detector has been biased in different working points, and illuminated by a ^{55}Fe radioactive source. Each pulse produced has been then analysed. Some results about the time parameters are shown in Fig. 2.
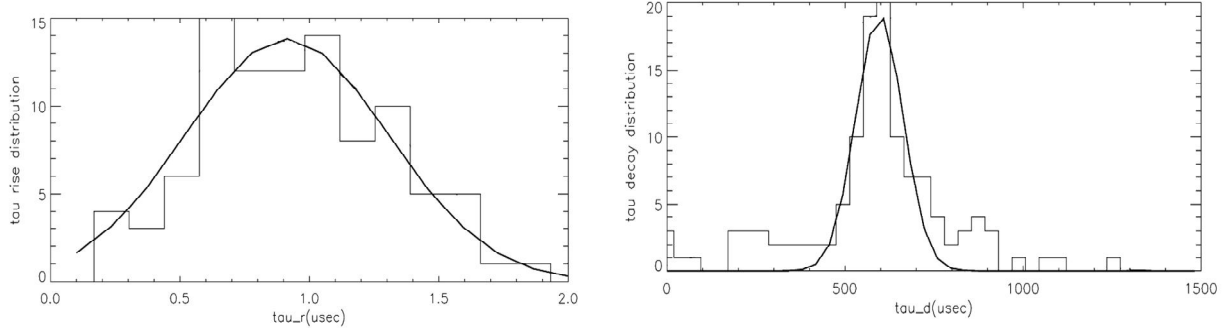
Figure 2: (Left) Rise time constant. (Right) - Decay Time constant.

The results are consistent for a typical mixed-regime: rise time driven by the a-thermal pulse (very fast ~ 1 μs, one order of magnitude faster than the value expected for a thermal pulse), and decay time driven by the thermal pulse (hundreds of μs, evaluated as from Ref. [10]). In fact, this is also independently demonstrated in Fig. 3. In the left panel we show a single component does not fit the data, that requires of a double pulse. In addition, we also note that the longer (thermal) component has a rise time of about 30 μs, similar to the decay time of the faster (a-thermal) component, consistently with the expected behaviour.
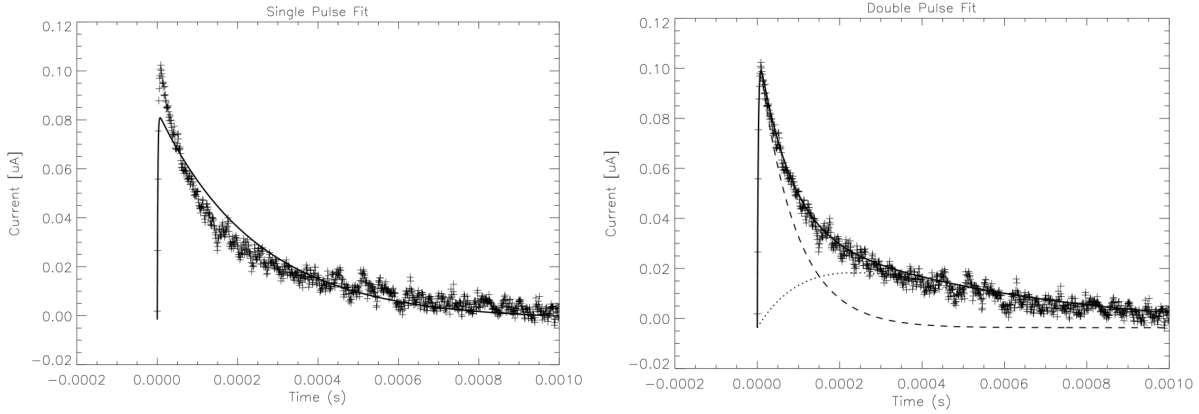

Figure 3: (Left) Example of single pulse Fit. (Right) Example of double pulse Fit.

In Fig. 4 we show the spectrum where the x-axis gives the energy deposited in the absorber (computed as from [10]):
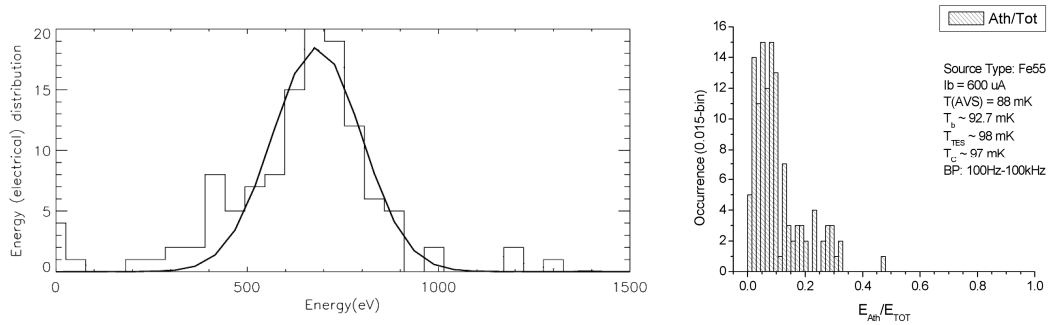

Figure 4: (Left) The spectrum of the deposited energy (source ^{55}Fe). (Right) A-thermal-to-Total energy ratio.

The energy deposited is a factor ~ 10 lower than expected by a thermal behaviour. This behaviour is expected due to the large value of G, a factor of 10 times larger than typically adopted. We thus expect that a significant fraction of the thermal pulse will be dumped into the bath. The energy resolution at 6 keV is (1σ) 100 eV (25% FWHM) comparable to the 1σ noise of 75 eV from the baseline r.m.s. We have also performed an analysis of PH distributions from double pulse fitting procedure. In Fig. 4 (Right) we show the ratio of a-thermal vs total energy deposited in the absorber. The average

value is about 5%. Given that the thermal component is depressed by a factor of 10, we thus estimate that for this sample the relative amplitude of the a-thermal component is around 0.5%, consistent with other measurements.

3.2 Prototype Detector AC-s2

The next Fig. 5 shows the first sample we obtained withe an area of 1cm^2. Some physical and geometrical parameters are shown in Table 2.

Figure 5: The 1 cm squared detector. See text for details. From the Left: Detector, stress dumper, bondings.

The surface of the detector has been covered by 4 TES to better collect the a-thermal phonons, each TES has been padded by thin (400 nm) Al films. The Al pad increases the effective collecting area, since the quasiparticles produced by high energy phonons diffuse towards the TES giving an additional heat signal. The absorber has been mounted on the top of a silicon chip which acts as dumper of the mechanical stress induced by the thermal cycle during the cooling (Fig. 5 middle). So, the sample has been glued on such a substrate by means of 4 posts (MGO + GE 7031 glue) that realizes the thermal conductance between the absorber and the thermal bath. Then the TES have been electrically connected in "parallel" configuration for biasing and to get the signal (Fig. 5 Right).

The transition R-T is shown in Fig. 6 (Left). As shown, the full transition is broad (~ 45 mK), but it is composed by two transition (T_{c1} ~ 180 mK, and T_{c2} ~ 210 mK) with two normal state resistances value of R_{N1} ~ 13.5 Ω, and R_{N2} ~ 35 Ω, respectively. The shape of the transition is out of standard for typical TES, and the normal resistances is too high. the problem was due to an excess of O-plasma etching for removal of PMMA (polymethylmethacrylate resist) (5x std time), which in turn, produced an etching of the Ir TES. This sample offers nonetheless interesting features, such as a large transition (that should increase the E_{max}) with still large values of alpha. We have therefore investigated further the performances of this detector. I-V curves have been acquired to set working points (Fig. 6-Right).
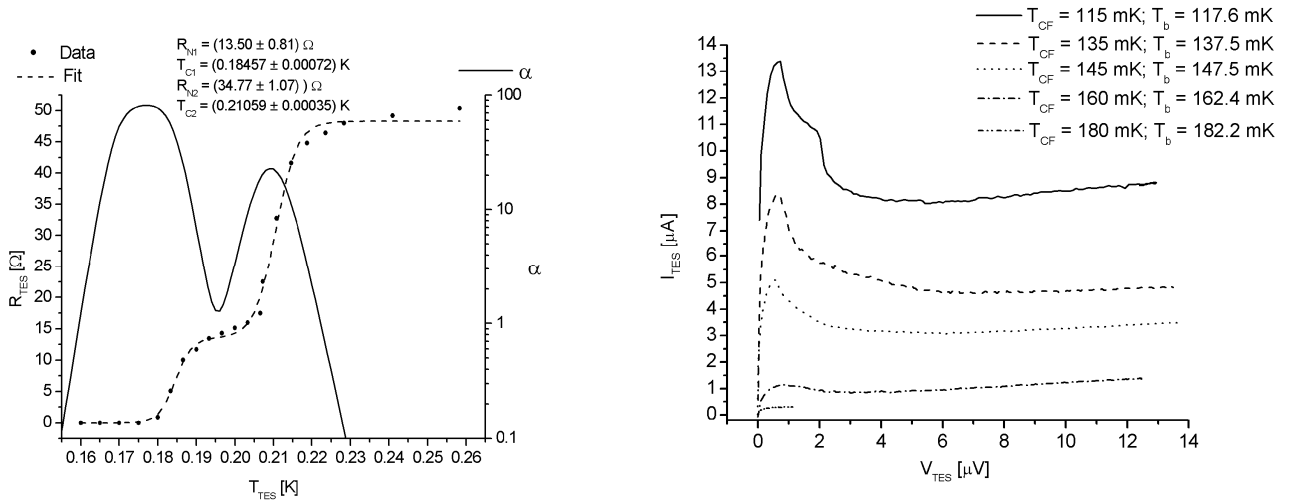

Figure 6: R-T and I-V measurements. -Left- Alfa (solid line) has been evaluated by a double transition fit (dashed line)- Right-. Temperature increase from top to bottom.

To evaluate the alpha parameter a fit which accounts for a double transition has been done. As expected two regime are shown. The value at the base of the first transition is as high as 100.

Tests have been done illuminating the detector with the sealed [241]Am radioactive source. The output signal has been amplified and filtered with a band-pass (100Hz-100kHz) to increase the S/N ratio. In front of the radioactive source has been put a copper plate, 500 μm thick, to shield all the photons excepted for the 59.54 keV line, and also to reduce the radiative input to the TES from the source material itself that cannot be properly cooled. The detector has been biased at T_b = 147 mK (V_{TES} ~ 1.5 μV; I_{TES} ~ 4 μA; P_{TES} ~ 6 pW). The following preliminary analysis have been done by considering a threshold equal to 10·σ, where 1σ is the rms-noise of the pulse baseline. The results about the Time constant decay and the Rise time are shown in the following Fig. 7.
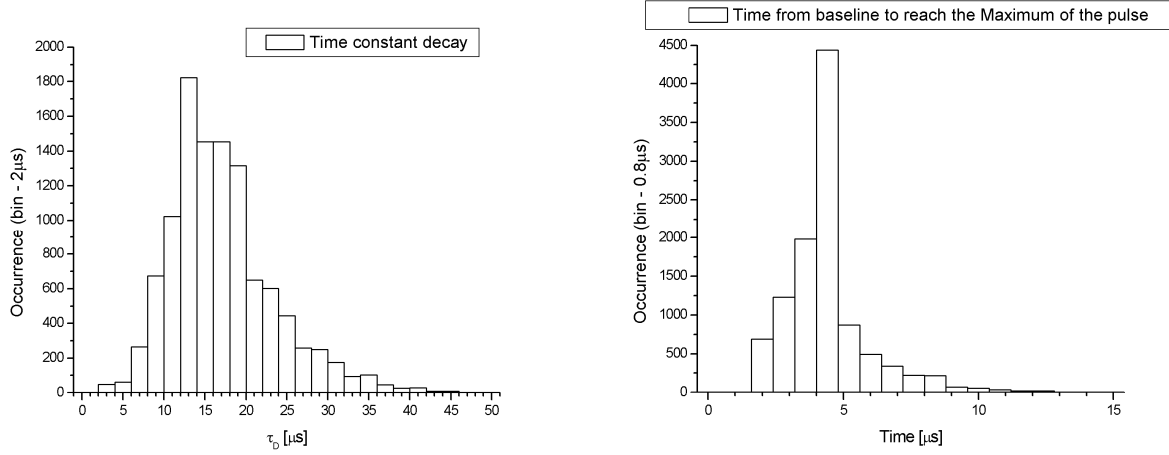

Figure 7: (Left) Time Constant Decay. (Right) Rise time (0%-100%).

The "τ" of the high pass filter is ~ 1.6 ms. From Table 2, the expected thermal time constant is evaluated as 270 ms, that is, the thermal pulse is cut away by the filtering section, even when the ETF is considered. The observed pulses are very fast. The average time constant decay is about 15 μs, and the average rise time constant (τ_R) is lower than 2 μs, as expected for a-thermal pulses. The distributions are narrow, so highlighting that the detector is working in the full a-thermal regime. In Fig. 8 we show the spectrum where the x-axis is the SQUID Voltage output, which in turn is related to the energy deposited in the absorber.
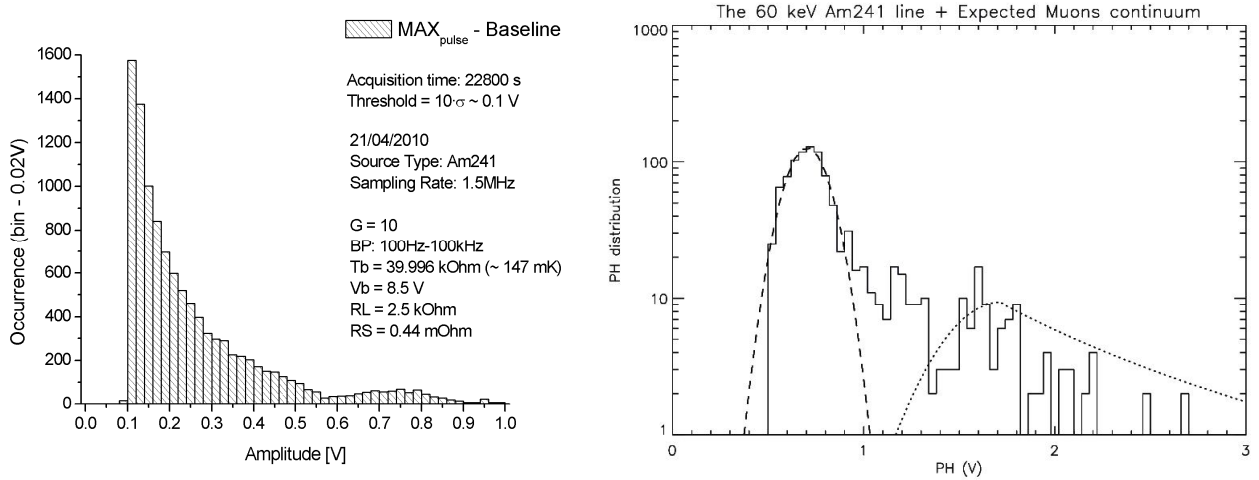

Figure 8: (Left) PH Distribution. (Right) - Dashed line- Fit of the 60 keV line. - Dotted line - Expected continuum from Muons which accounts for the detector energy resolution.

The PH distribution shows a broad line around 0.75 V, produced by 60 keV photons, and a low energy tail that is cut off by the threshold at 10 keV. In Fig. 8-Right a Gaussian fit to the line (dashed) is shown. The resolution (FWHM) at 60

keV is ~ 35 %. As far as the muons are concerned, the rate expected at these latitudes is of 0.5-0.8 cts/cm^2/min. The minimum deposited energy is evaluated for MIPs: dE/dx ~ 0.4 keV/um → E_{min} (380 um) ~ 145 keV ~ 1.74 V). Folding with the detector energy resolution, the expected PH distribution of the muons is shown in Fig. 8-Right as dotted line, roughly consistent with the data. We estimate E_{MAX} from the the first transition (Fig. 6), taking a resistance in the normal state ~ 13.5 ohm. From the working point (V_{TES} ~ 1.5 µV, R_{TES} ~ 0.39 Ω) and scaling by the 60 keV line (~ 0.3 µA), we derive E_{MAX} ~ 0.75 MeV. We stress that this is the bandwidth related to the a-thermal phonons. In conclusion, both the energy range and the pulse duration satisfy the requirements, however the low energy tail needs to be clarified.

The origin of this feature is attributed to the detector. We do expect in our set up, low energy component due to Cu fluorescence and Compton backscattering produced by 60 keV photons on the supporting structure. The expected count rate (verified also via GEANT4 simulations) should be few times larger than the count rate measured at 60 keV. In Fig. 9 we show the expected contribution from the fluorescence Cu line (K_α = 8.048 keV) assuming a line with the same (relative) resolution measured at 60 keV. Clearly, the measured count rate is much larger than predicted.
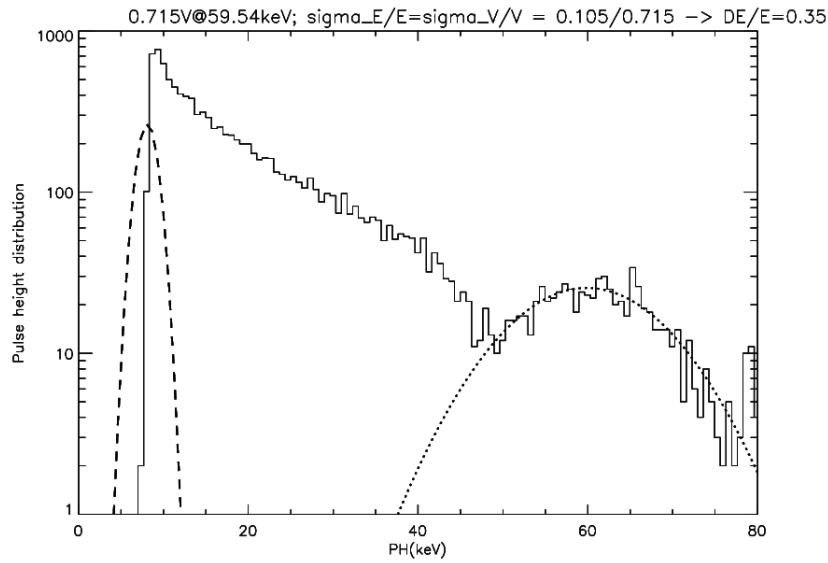

Figure 9: (Dashed line) Expected Copper K_α fluorescence line. (Dotted line) 60 keV line.

We think that the tail is related to a not-uniform operation of the detector due to the bimodal transition curve and/or different temperatures of the single TES films, inducing slightly different working points. The second higher temperature transition could be related to some part of the sensor film in series to all or some TES. So, the corresponding bias currents are modulated by the 4 TES with a different weights and the pulse heights are consequently different. This effect jeopardizes the point by point response function of the detector over the full surface. Since the a-thermal phonon goes across the crystal as quasi-ballistic mode, not only the solid angle subtended by the hot spot inside the crystal towards the TES must be maximized, but also the response of the TESs must be uniform.

We have therefore improved the process for the manufacturing of another detector, AC-s3.

3.3 Prototype Detector AC-s3

A third sample has been produced, with a lower normal resistance, so covering up to 3 order of magnitude from Ac-s1 to Ac-s3, and with a better control of the manufacturing processes. It is similar to the AC-s2 sample (1 cm^2, 4 TES). The differences are related to the Al-pads (Fig. 10 Left) that here, to guarantee the in-parallel readout and to collect more quasi-particles, cover as strip one couple of TES, to the Ir thickness, and finally, to the presence of Au deposition to lower the transition temperature.

The transition R-T is shown in Fig. 10. As shown, it is well shaped and narrow (~ 2 mK), and the normal state resistances value is ~ 55 mΩ. To evaluate the alpha parameter a fit has been done. The maximum value is as high as 300. The I-V curve are shown in Fig. 11.

A background spectrum has been acquired with the following operating parameters: Gain and bandpass of amplifier (G = 2, 10Hz-30kHz); working point at T_b ~ 132 mK (V_{TES} ~ 0.7 μV; I_{TES} ~ 37 μA; P_{TES} ~ 26 pW); noise threshold at 0.08 V that corresponds to 4·σ value (1σ ~ 0.02 V). The spectrum is shown in Fig. 11-Right.
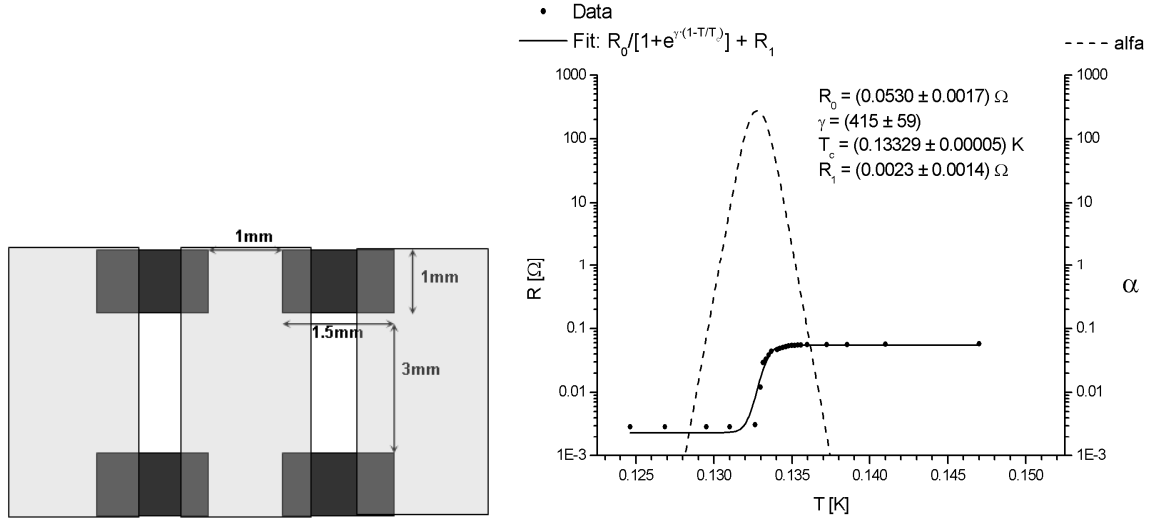

Figure 10: (Left) AC-s3 detector Scheme: the Al pads (light gray) are laid upon TESes (black). (Right) R-T and alfa curves.
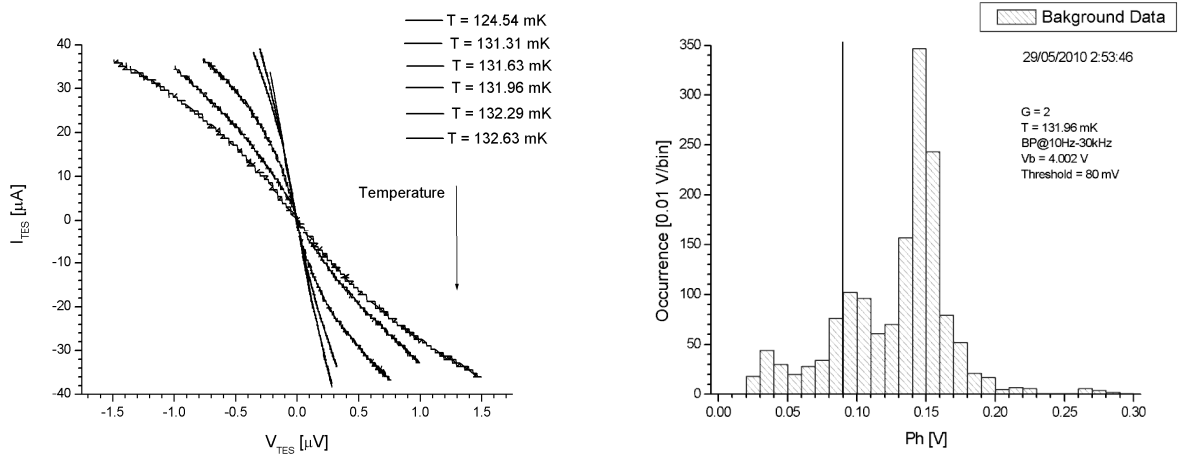

Figure 11: (Left) I-V curves. (Right) Background Spectrum. The vertical line is the set threshold.

Above the threshold there is a line centered at ~ 0.14 V. It is attributed to fluorescences induced by muons that hit the sample holder close to the detector.

The detector has been then illuminated by the sealed [241]Am source and biased in the same working point used for the background. The results about the time constants are shown in the following Fig. 12.
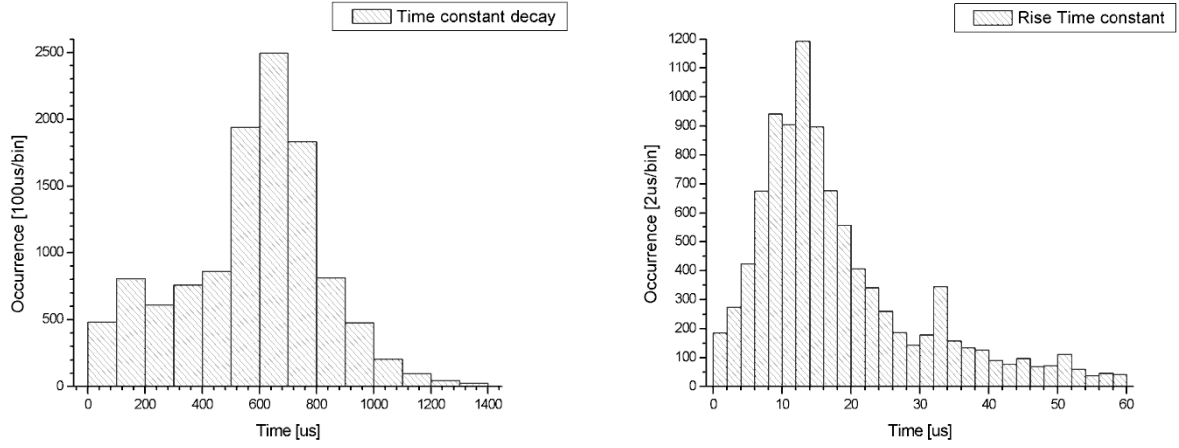
Figure 12: (Left) Time constant decay. (Right) Rise time constant.

Since the used Supracon SQUID input coil inductance is about 350 nH, due to the low resistance a cutoff around 10 kHz for this set point is expected. The athermal component is therefore cancelled out by the filter. The cutoff due to L_{in} is evident in the next plot (Fig. 13) where the detector noise, mainly the Jhonson noise, has been acquired not filtered and in no-bias condition.
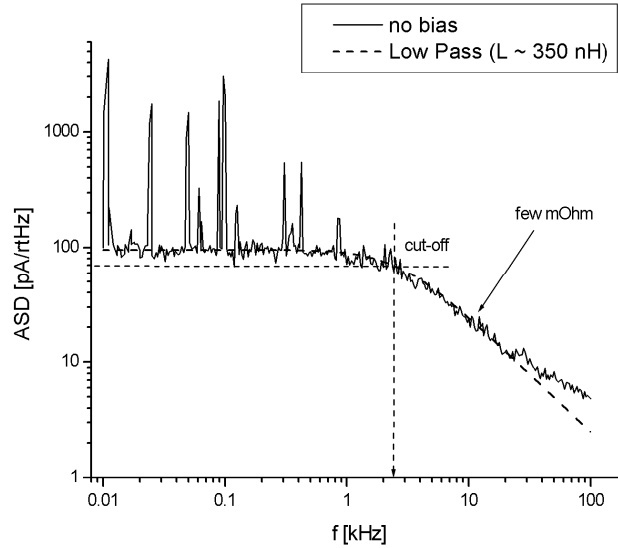

Figure 13: Noise spectrum.

In addition, the rise time constant is close to the expected value from the L/R filter, $Tau_{L/R} \sim 18$ μs. The expected value of the thermal time constant is about 5.5 ms. By taking into account the evaluated loop gain L ~ 2, the $Tau_{ETF} \sim 1.8$ ms, which is a factor 3 greater than the measured value. The factor of 3 discrepancy with the measured value is consistent with the present uncertainties in the values of G and C.

Limitation in the maximum current that can be stand by the present SQUID set up has limited the choice of a working point farther from the transition temperature, desirable to increase the ETF. We plan to explore this region of working points with a future upgrade of the set up. We also plan to implement a Magnicon (PTB) SQUID, characterized by a much lower input inductance, that will allow to measure the fast a-thermal pulse.

The spectrum produced by illuminating the detector with 60 keV photons is shown in Fig. 14.

The excess close to the threshold is very likely due by a combination of fluorescence and Compton backscattering produced by 60 keV photons. We expect a contribution extending up to about 30 keV (including the effect of the poor energy resolution) with a count rate several times larger than that of 60 keV photons in the present sample of Si absorber (that has a photoelectric absorption efficiency of about 2%). The rather broad energy resolution displayed by the 60 keV line, centered around 0.2 V, indicates that the detector response is not much uniform, thus we cannot exclude the possibility that some fraction of 60 keV photons are indeed contributing to the lower energy excess. This is again not unexpected, because, as it was the case for AC-s1, we are operating this detector in a depleted thermal regime (note, in fact, the similar high value of G for the two detectors – Table 2), because our goal was to maximize the a-thermal component. As mentioned above, we plan to switch to an input coil with a lower inductance to measure the fast a-thermal pulse. The energy spectrum scaled by the 60keV@0.2V is shown in Fig. 14-Right.
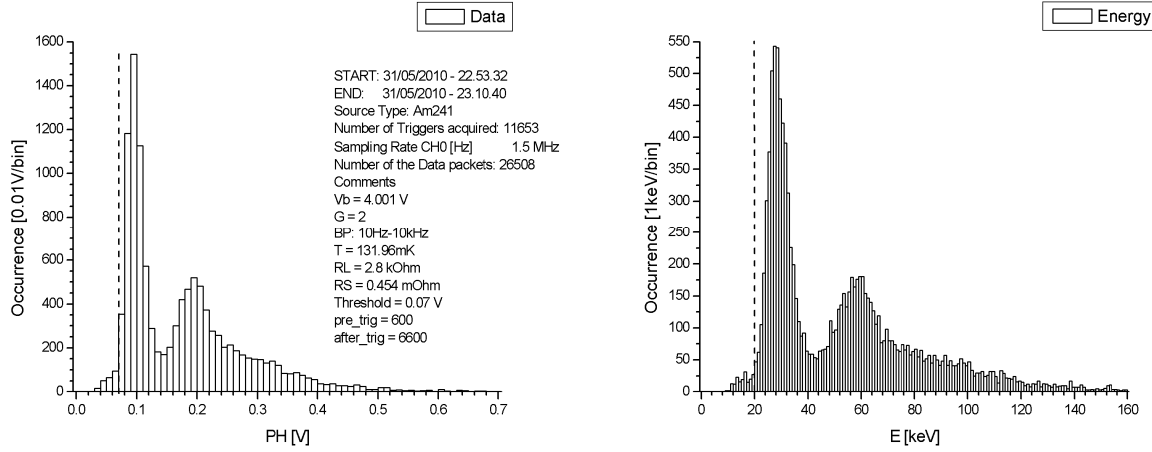

Figure 14: (Left) PH Distribution. The dashed-line is the threshold. (Right) Energy spectrum of 60 keV [241]Am source.

The detector threshold is around 20 keV. By using only the transition measurement, it is possible to estimate the energy bandwidth by taking into account the expected normal Resistance ~ 0.55 ohm. So, by adopting the same working point of the previous run and scaling by the 60 keV line (~ 0.42 µA), we derive E_{MAX} ~ 3.1 MeV.

4. CONCLUSIONS

The following Table 3 highlights the main results of the 3 detectors developed.

Table 3: Measured performances of the detectors. Notes: [1] 5 sigma noise. [2]: including the area of the Al pads. [3]: ratio of the collecting TES area to the total area of the absorber

Detector	Absorber area (mm^2)	Thickness (µm)	TES[3] fractional collecting area (%)
AC-s1	16.5	300	11
AC-s2	100	380	9[2]
AC-s3	100	380	17

Detector	Rise time (τ – µsec)	Decay time (τ – µsec)	Emin[1] (keV)	Emax (keV)	Comments
AC-s1	<1 (F) 30(S)	80 (F) 600 (S)	3	460	F,S= fast and slow components
AC-s2	<1	20	5	800	a-thermal
AC-s3	15	600	20	3100	Thermal

With the three prototypes we have covered a wide range of parameters, in area, resistance, and qualified a read out method based on multi-TES readout that allows to increase the collecting area in order to maximize the a-thermal (fast)

pulse. In fact, we have successfully observed this component, that is characterized by a rise time of the order of 1 μs and a decay time of about 20 μs both in the small (AC-s1) and large (AC-s2) detectors. Both the time constants and the amplitude are consistent with expectations though for AC-s2 the energy spectrum is indicating a not-uniform response This has been cured with the third detector, AC-s3. With the present set-up the AC-s3 detector shows a predominant thermal pulse. Nonetheless, it is meeting the requirements in term of bandpass and pulse rise time while the decay time is longer. However, the fast a-thermal pulse that is expected for this sample, will easily meet the requirements. We plan to test this sample with a larger bandpass by using a different SQUID with a lower value of L as well as a larger value of TES bias current, that in the present set-up, has limited the temperature of the bath to be close to the operating point. We also plan to improve both the TES-coverage and uniformity, that should reflect into a better energy resolution particularly for the a-thermal component. We have actually already manufactured a detector (AC-s4) of 1.5 cm^2 with 8 TES sensors.

Moving a further step forward towards a form–fitting prototype, we plan then to upscale the area to 18x18 mm^2. Considering the consistency and predictability of the performances over the large range in area already covered by the present prototypes, we do not foresee any significant problem to achieve the area of the baseline design. This form fitting prototype will meet also the thermal, mechanical and electrical interfaces thus we plan, e.g., to achieve a good control on the manufacturing of a calibrated G.

REFERENCES

[1]   IXO, http://sci.esa.int/science-e/www/area/index.cfm?fareaid=103; http://ixo.gsfc.nasa.gov/
[2]   A. Parmar, "IXO - The International X-ray Observatory", Proc. Of Science, PoS(extremesky2009)077, (2009).
[3]   K. D. Irwin and G. C. Hilton, "Cryogenic particle detection", C. Enss Edition, Springer-Verlag Berlin Heidelberg (2005)
[4]   C. Macculi et al., "TES Microcalorimeter for IXO: from Focal Plane to Anticoincidence detector", Proc. Os Science, PoS(extremesky2009)086, (2009).
[5]   L. Colasanti et al., "Development of a TES based Cryo-Anticoincidence for a large array of microcalorimeters", AIP Conference Proceeding, 1185, 438-441 (2009).
[6]   F. Gatti, D. Bagliani et al, "Fabrication and characterisation of TES anti-coincidence cryogenic detector for IXO", this Volume
[7]   E. Perinati et al., "Study of the background for the X-Ray Microcalorimeter Spectrometer on board the International X-Ray Observatory", this Volume
[8]   M. R. Hauser et al, "Imaging phonons in a superconductor", Phys. Rev. B 60, 3072–3075 (1999)
[9]   M. E. Msall, J. P. Wolfe, "Ballistic phonon production in photoexcited Ge, GaAs, and Si", Phys. Rev. B 65, (2002).
[10]   Y. Takei et al., "Performance of a bridge-type TES microcalorimeter, excess noise characteristics and dependance of sensitivity on current", NIM-A, 523, 134-146, (2004).